



Effect of retained austenite – Compressive residual stresses on rolling contact fatigue life of carburized AISI 8620 steel



Yi Shen^a, Sina Mobasher Moghadam^a, Farshid Sadeghi^{a,*}, Kristin Paulson^b, Rodney W. Trice^b

^a School of Mechanical Engineering, Purdue University, West Lafayette, IN 47907, USA

^b School of Materials Engineering, Purdue University, West Lafayette, IN 47907, USA

ARTICLE INFO

Article history:

Received 11 September 2014

Received in revised form 10 February 2015

Accepted 22 February 2015

Available online 4 March 2015

Keywords:

Rolling contact fatigue

Retained austenite

Compressive residual stresses

Continuum damage mechanics

ABSTRACT

In this study the rolling contact fatigue (RCF) of case carburized AISI 8620 steel was numerically and experimentally investigated. For the numerical study, a two dimensional finite element (FE) RCF model based on the continuum damage mechanics (CDM) was developed to investigate the fatigue damage accumulation, crack propagation and final fatigue life of carburized AISI 8620 steel under various operating conditions. A randomly generated Voronoi tessellation was used to model the effects of material microstructure topology. The boundaries of the Voronoi elements were assumed to be the weak planes where damage accumulates, cracks initiate and propagate to simulate inter-granular cracks. A series of torsional fatigue tests were conducted on carburized AISI 8620 steel specimens containing 0% and 35% retained austenite (RA) to determine fatigue load (S) vs. life (N) of the material. The S–N results were then used to determine the material parameters necessary for the rolling contact fatigue model. The torsional fatigue test results indicate that the carburized AISI 8620 specimens with higher RA demonstrate higher life than the specimens with lower RA. The RCF model also indicates that the material with higher level of compressive residual stresses (RS) and retained austenite demonstrates higher RCF life. In order to corroborate the results of RCF model, a three-ball-on-rod rolling contact fatigue test rig was used to determine the RCF lives of carburized AISI 8620 steels with different amounts of RA. The fatigue life and cracks evolution pattern from the numerical and experimental results were corroborated. The results indicate that they are in good agreement.

© 2015 Elsevier Ltd. All rights reserved.

1. Introduction

Heavily loaded non-conformal machine components such as bearings and gears are commonly subject to rolling contact fatigue. RCF manifests through a variety of failure modes [1] but the most widely observed phenomena are surface or subsurface originated spalling, as shown in Figs. 1 and 2. The former is due to the surface irregularities (such as dent) on the mating bodies where cracks initiate and then propagate downward into the material. The final formation of shallow craters is referred to as surface pits. In the latter case, cracks are initiated below the contacting bodies and propagate upwards to create spalls on the surface. Modern machinery commonly use high-quality bearings which have superior surface finishes and operate in the presence of clean lubricants;

under these circumstances, subsurface originated spalling mechanism is dominant [2].

Contrary to the classical fatigue (bending, torsion, etc.) which is dominated either by normal or shear stress, rolling contact fatigue is a multi-axial fatigue problem. Fig. 3 depicts the stresses history at the depth of $0.5b$ (b is the half contact width) below the surface in a plane strain RCF case. The only alternating stress observed is shear stress and thus rolling contact fatigue is considered as a shear driven phenomenon, as postulated by Lundberg and Palmgren [3].

Rolling contact fatigue has been the subject of significant investigation since the early 1940s [4,5]. In order to improve RCF behavior, heat treatments have been commonly used to induce compressive residual stresses within the material. A number of investigators have studied the effects of compressive residual stresses on rolling contact fatigue. These studies as expected demonstrated that fatigue lives can be improved when the bearing material contains some level of compressive residual stresses. Cretu and Benchea [6] used 6308 deep-groove ball bearings to conduct rolling contact fatigue experiment and his results revealed

* Corresponding author. Tel.: +1 765 4945719.

E-mail addresses: shen145@purdue.edu (Y. Shen), smobashe@purdue.edu (S.M. Moghadam), sadeghi@ecn.purdue.edu (F. Sadeghi), kpaulson@purdue.edu (K. Paulson), rtrice@purdue.edu (R.W. Trice).

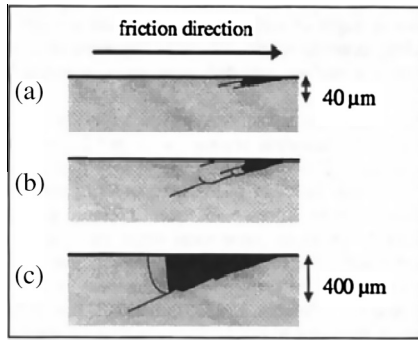


Fig. 1. Surface originated pitting.

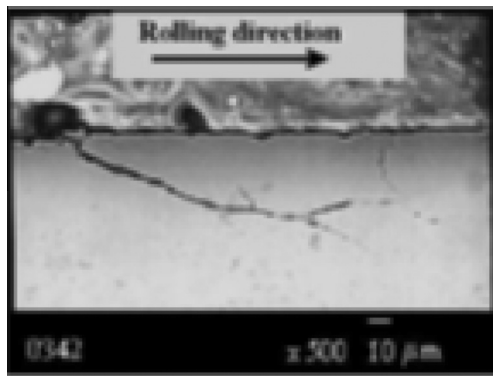


Fig. 2. Subsurface originated spalling.

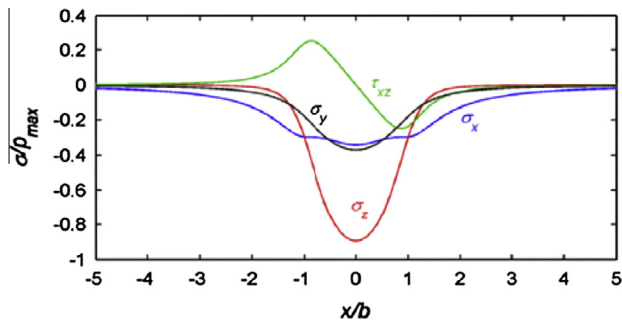


Fig. 3. Rolling contact fatigue stresses history under plane strain condition.

that compressive residual stresses increased the fatigue life. Chen et al. [7] used fracture mechanics to investigate mode II failure in rolling element bearings (REB) and found that residual stresses reduced the value of ΔK_{II} in high cycle fatigue, thus lowering the crack propagation rate. Guo [8] proposed that residual stress profiles improve the condition of near-surface initiated rolling contact fatigue. Typically, RCF models account for either the crack initiation or propagation phase but rarely both. Liu and Choi [9–11] developed a fracture mechanics based model including both crack initiation and propagation lives to investigate the effects of residual stresses scatter on rolling contact fatigue. The model confirmed the positive effects of compressive residual stresses on RCF behavior of AISI 1053 steel. The idea that compressive residual stresses might benefit fatigue behavior of material was applied by Prevey and Jayaraman [12] in his design methodology for gas turbine engine components.

Retained austenite is the austenite that does not transform to martensite upon quenching. The presence of retained austenite

in material has a direct influence on the fatigue behavior of rolling element bearings. A number of investigators have studied the effect of retained austenite on rolling contact fatigue. Zhu et al. [13] carried out RCF experiments on 18Cr2Ni4WA steel with different amounts of retained austenite. He found that the contact fatigue resistance increases with larger amount of retained austenite. Dommarco et al. [14] investigated the influence of retained austenite on the RCF behavior of SAE 52100 steel and found that under the same distribution of residual stresses, specimen with larger volumetric fraction of retained austenite shows a superior fatigue resistance. Zheng et al. [15] studied RCF of carbide-free bainitic steel and determined that the specimens with higher levels of RA possessed better RCF performance.

Silva et al. [16] conducted four point bending fatigue and wear tests on carburized SAE 8620 steels with different levels of retained austenite. His results showed that specimen with higher amount of RA exhibited longer fatigue life. Prado and Arques [17] designed a similar bending test and found an optimum austenite content that would result in the highest fatigue endurance is about 20–30%. A series of S–N results for transformation induced plasticity (TRIP) steels with different amounts of RA (0–11.5%) were presented by Abareshi and Emadoddin [18]. The results illustrated that the highest level of retained austenite (11.5%) exhibits the longest life. However, Hu et al. [19] pointed out that austenite would accelerate fatigue propagation due to the strain-induced martensitic transformation. Herring [20] indicates that in order to avoid significant volume change of the components that the level of RA should be less than 10%.

The aim of this study is to numerically and experimentally investigate the effects of retained austenite and residual stresses on rolling contact fatigue. The material used in this investigation is case carburized AISI 8620 steel, which is commonly used for non-conformal contacts such as bearings, cam and followers. A two dimensional FE RCF model was developed to investigate the fatigue behavior of the material. The damage law was modified based on the Goodman equation to incorporate the effects of RS in the material. A randomly generated Voronoi tessellation was used to model the effects of material microstructure topology. The boundaries of the Voronoi elements were assumed to be the weak planes where damage accumulates, cracks initiate and propagate. Torsional fatigue tests were conducted to obtain material parameters for the RCF model. The results demonstrate that higher level of RA is beneficial in increasing fatigue life. Three-ball-on-rod RCF tests on carburized AISI 8620 steels with different amounts of retained austenite were conducted to verify the results from RCF model. The fatigue life and cracks evolution pattern in both numerical and experimental investigations were corroborated, and the results show that they are in good agreement.

2. Modeling approach

2.1. FEM model

ABAQUS finite element software was used to develop a plane strain RCF model based on the continuum damage mechanics. The model was used to investigate the effect of compressive residual stresses on RCF phenomenon. Fig. 4 schematically illustrates the set-up of the FEM model. In non-conformal Hertzian contact, the half contact width is only a few hundred microns and most of the subsurface cracks are originated within this region. Therefore, the Hertzian semi-infinite domain with dimensions $10b \times 7b$ ($b = 100 \mu\text{m}$, the half contact width) in the rolling (x) and transverse (y) directions, respectively was selected as the simulation domain. A Hertzian pressure described by Eq. (1) is moved over the top of the domain in 21 discrete steps. The application of

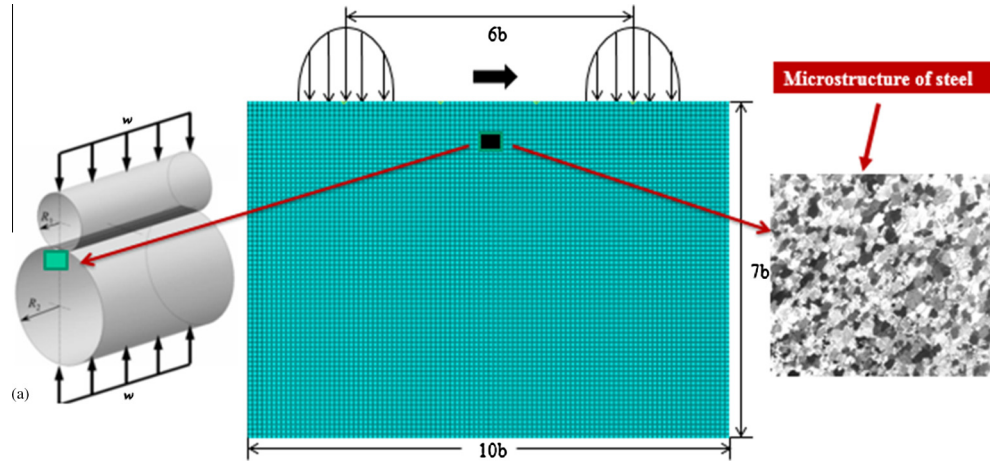


Fig. 4. The rolling contact fatigue simulation model.

the Hertzian pressure, which is in the form of surface traction is achieved through the user defined subroutine UTRACLOAD.

$$p = p_{\max} \sqrt{1 - \left(\frac{x}{b}\right)^2} \quad (1)$$

where p_{\max} is the maximum Hertzian pressure.

During the simulation, the entire domain is subject to damage however; predominately cracks only initiate and propagate in the area near the center of the contact domain where the reversal shear stress is the largest. In this specific region, or representative volume element (RVE), Voronoi cells [21] were implemented, as shown in Fig. 5. In the Voronoi tessellation, the space is divided into many regions such that all points in each region are closer to the seed point of that region compared to the seed points of other Voronoi regions. Each Voronoi cell represents a material grain with random shape and orientation. The average size of the Voronoi element is set equal to the grain size observed in bearing steels, which is around 10 μm . As shown in Fig. 5, the microstructure of bearing steel exhibits a granular pattern with a high-degree of randomness. Therefore, the Voronoi tessellation was used to simulate the microstructure of steel materials as described by [2,21–26]. To represent different microstructures of carburized AISI 8620 steel, 33 domains were created with randomly generated Voronoi mesh in the RVE region. For the rest of the domain, a triangular constant strain element (CSE) was applied.

2.2. Damage mechanics incorporating effects of residual stresses and retained austenite

In the past few decades, damage mechanics has been extensively applied to fatigue problems [22–32]. In damage mechanics, the material is degraded by accumulation of damage. Eventually the material is completely damaged, resulting in a loss of effective

area (in 2D) or volume (in 3D) that resists the load. Kachanov [33] defined the damage variable as:

$$D = \frac{A - A^*}{A} \quad (2)$$

where D is the damage variable, ranging from 0 to 1. When $D = 0$ material is undamaged and when $D = 1$, material is fully damaged. A and A^* are the pristine undamaged and damaged areas, respectively.

The damage evolution as a function of cycle is given by Xiao et al. [34]:

$$\frac{dD}{dN} = \left(\frac{\sigma_a}{\sigma_r(1-D)}\right)^m \quad (3)$$

where N is the number of cycles, σ_a is the critical alternating stress component causing fatigue damage, σ_r and m are material parameters.

In order to determine the fatigue life N_f , Eq. (3) is integrated, resulting in:

$$N_f = \left[\frac{\sigma_a}{(m+1)^{-\frac{1}{m}}\sigma_r}\right]^{-m} \quad (4)$$

Now considering Basquin's law [35] given by:

$$\sigma_a = C(N_f)^{-\frac{1}{B}} \quad (5)$$

where B is a material related parameter and C is a function of mean stress caused by the existence of residual stresses.

Modifying the Basquin's law based on Goodman equation [36,37] to include the effect of mean stress we obtain;

$$\sigma_a = C_0 \left(1 - \frac{\sigma_m}{S_{ut}}\right) (N_f)^{-\frac{1}{B}} \quad (6)$$

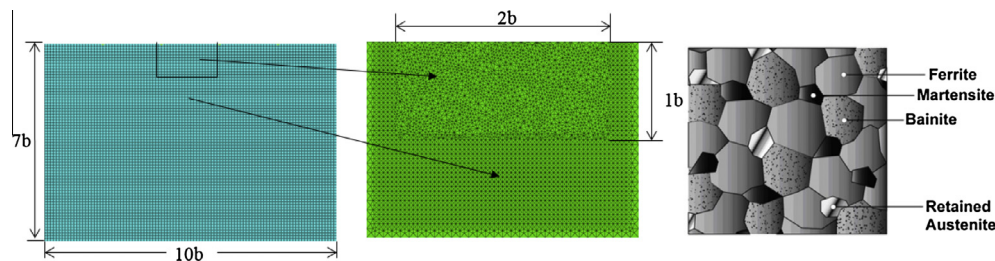


Fig. 5. Voronoi mesh in RVE area and granular feature of steel microstructure.

Rearranging Eq. (6) we obtain;

$$N_f = \left(\frac{\sigma_a}{C_0 \left(1 - \frac{\sigma_m}{S_{ut}}\right)} \right)^{-B} \quad (7)$$

where S_{ut} is the ultimate stress and C_0 is the constant in the Basquin's law determined by testing at zero mean stress.

Equating Eqs. (4) and (7), rearranging and simplifying we obtain:

$$\left[\frac{\sigma_a}{(m+1)^{\frac{1}{m}} \sigma_r} \right]^{-m} = \left[\frac{\sigma_a}{C_0 \left(1 - \frac{\sigma_m}{S_{ut}}\right)} \right]^{-B} \quad (8)$$

Comparing terms on the left and right sides of Eq. (8), we will obtain,

$$m = B$$

$$\sigma_r = C_0 \left(1 - \frac{\sigma_m}{S_{ut}}\right) (m+1)^{\frac{1}{m}}$$

Letting

$$\sigma_{r0} = C_0 (m+1)^{\frac{1}{m}}$$

$$\sigma_r = \sigma_{r0} \left(1 - \frac{\sigma_m}{S_{ut}}\right) \quad (9)$$

Now the damage law equation can be written as:

$$\frac{dD}{dN} = \left(\frac{\sigma_a}{\sigma_{r0} \left(1 - \frac{\sigma_m}{S_{ut}}\right) (1-D)} \right)^m \quad (10)$$

where in this equation, σ_{r0} , S_{ut} and m are material dependent parameters. Once the S–N results for a particular steel is obtained from torsion fatigue test, the damage evolution rate of the steel is determined through Eq. (10).

The stress component responsible for fatigue failure is case dependent. As described previously, both the torsion and rolling contact fatigue are shear driven phenomenon. Therefore, the alternating stress component in the damage evolution rate is chosen as the shear stress reversal $\Delta\tau$ and thus Eq. (10) is modified to:

$$\frac{dD}{dN} = \left(\frac{\Delta\tau}{\tau_{r0} \left(1 - \frac{\sigma_m}{S_{us}}\right) (1-D)} \right)^m \quad (11)$$

where τ_{r0} is the material parameter and σ_m represents the mean stress due to the presence of residual stresses.

2.3. Integration of FEM model and damage mechanics

ABAQUS FE software was used to develop the continuum damage mechanics RCF model in this investigation. In order to corroborate the experimental and numerical results, the semi-infinite domain was subject to a uniform compressive residual stresses state given by residual stresses measurement. The model was also used to investigate the effect of a larger compressive residual stress [9] on fatigue.

At the beginning of the simulation, the value of damage in every element is set to zero, representing undamaged state of the pristine domain. Then a “jump-in-cycles” (JIC) algorithm [38] was applied. The principle of this method is to assume the damage is kept a constant value over a cycle increment ΔN and damage will only be updated at the end of each increment. A detailed introduction to this algorithm was given by Weinzapfel and Sadeghi [2] and this method was also applied in [21–26]. Once the value of damage

reaches one, the element will be fully damaged and crack forms along the element boundary. The final failure occurs when the crack reaches the surface of the domain, forming spall as depicted by Fig. 2. The final life and spall pattern are recorded to compare with experimental results from three-ball-on-rod test.

2.4. Torsion fatigue tests

The torsion fatigue test rig was used to determine the stress vs cycle (S–N) of torsion specimens with different levels of RA. The results from this test were used to obtain the material parameters used in the numerical model. In this investigation a standard MTS torsion fatigue test rig (Fig. 6) was used to obtain S–N results for carburized AISI 8620 steels with low (~0%) and high (~35%) RA. Fig. 7 illustrates the custom made grips used to hold the specimen. The MTS hydraulic rotary actuator applies angular displacement and the resultant torque is monitored by an in-line MTS torque cell. The custom grips [22] were developed to guarantee that the specimen is gripped properly without slip and no bending moment is generated in the specimen [23].

2.4.1. Torsion fatigue test specimen

The specimens for torsion fatigue tests are made of carburized AISI 8620 steel following ISO 1352 standard [39]. Fig. 8 illustrates a schematic of the specimen. All specimens were heat treated in one single carburizing cycle to target high retained austenite. This was achieved by high carbon potential in the furnace along with lowest possible tempering temperature to ensure all specimens end up with high retained austenite. After the carburizing cycle, the parts were divided into two batches, with one half of the parts going directly to final tempering and the other half going through deep freeze operation to convert retained austenite into martensite. The deep frozen parts were then tempered in the same fashion as the first half. Microstructurally, the specimens exhibit distinct case and core microstructures with total case depths (depth of dark etched area that differentiates case from core) were about 550 microns depth. Samples of the low and high RA carburized AISI 8620 materials were evaluated to determine the S–N for each material.

2.4.2. Torsion fatigue test procedure

Before conducting fatigue experiments, three static tests were carried out to determine the ultimate shear stress of each material. The maximum torque applied in the static tests was averaged and the mean value was used to obtain S_{us} according to:

$$S_{us} = \frac{T_{\max} r_{\min}}{J} \quad (12)$$

where S_{us} is the ultimate strength in shear, T_{\max} is the maximum torque, r_{\min} is the minimum cross section radius of the specimen and J is the polar moment of inertia.

For fatigue testing, the applied torque was varied between $0.3T_{\max}$ and $0.9T_{\max}$. Tables 1 and 2 contain the torques applied in the static and fatigue tests for low and high RA cases respectively. The stress amplitude τ_a in fatigue tests is calculated from

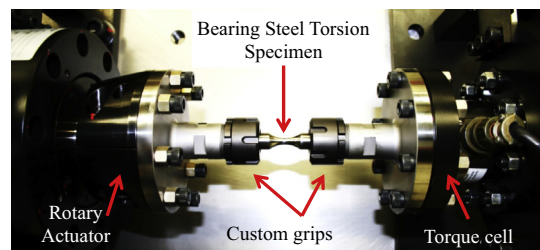


Fig. 6. MTS torsion fatigue test rig.

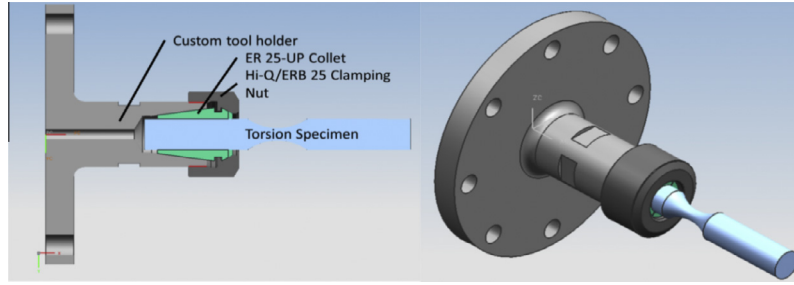


Fig. 7. Cutaway of the gripper and assembly.

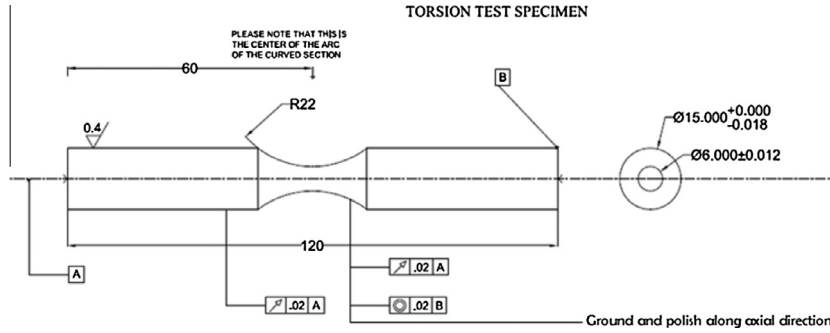


Fig. 8. Torsion specimen.

Table 1

Torques and corresponding shear stress levels of static and fatigue tests for carburized AISI 8620 steel (low retained austenite level).

	Static					Fatigue					
T_a (in-lbf)	577.6	519.8	462.0	404.3	375.4	346.5	317.6	288.8	259.9	231.0	173.2
τ_a (GPa)	1.54	1.38	1.23	1.08	1.00	0.92	0.85	0.77	0.69	0.62	0.46
τ_a/S_{us}	1.00	0.90	0.80	0.70	0.65	0.60	0.55	0.50	0.45	0.40	0.30

Table 2

Torques and corresponding shear stress levels of static and fatigue tests for carburized AISI 8620 steel (high retained austenite level).

	Static					Fatigue					
T_a (in-lbf)	672.5	605.3	538.0	470.6	437.1	403.5	369.9	336.3	302.6	269.0	201.8
τ_a (GPa)	1.79	1.61	1.43	1.25	1.16	1.07	0.99	0.90	0.81	0.72	0.54
τ_a/S_{us}	1.00	0.90	0.80	0.70	0.65	0.60	0.55	0.50	0.45	0.40	0.30

Eq. (12) by replacing T_{max} and S_{us} with fatigue test torque and corresponding stress amplitude respectively. To obtain a reliable S–N curve for each level of retained austenite, three tests at each stress level were conducted. All tests were conducted under room temperature. To detect the failure condition, the angular displacement of the specimen is recorded and when the displacement surpasses a threshold limit due to the fracture of the bar, the test is stopped and final life is recorded. The fatigue test results (not including static test results) were curve fitted using the power law equation and least squares method. The material parameters were calculated using the power law equation obtained and then applied in the RCF model.

3. Experimental investigation

A three-ball-on-rod RCF test rig was used in this investigation to experimentally assess the effects of retained austenite and residual stresses on RCF. The levels of RA and RS are measured using X-ray diffraction (XRD) technique. The three-ball-on-rod RCF test rig was used to determine the probability of failure for specimens with low or high levels of RA.

3.1. Three-ball-on-rod rolling contact fatigue tests

A three-ball-on-rod rolling contact fatigue test rig was used to evaluate the RCF behavior of carburized AISI 8620 steels with different levels of RA. Fig. 9 illustrates a test head, vibration table/monitoring system and running time recorder of the 3-ball-on-rod rolling contact fatigue rig employed in this investigation. The test head is used to hold, load and rotate test specimen. The rotating speed is 3600 rpm. Turbine oil (MIL-PRF-23699-STD) is used under room temperature (25 °C) to lubricate the contact. The accelerometer placed on the vibration table is used to detect the excessive vibration (0.5 RMS above the initial setting) and stop the test when the rod has formed a spall.

3.1.1. RCF test specimen

Fig. 10 illustrates the specimen, assembly and loading configuration. The test specimen is a 76.2 mm (3 inches) long, 9.5 mm (3/8 inch) diameter cylindrical rod made of case carburized AISI 8620 steel. All specimens came from the same heat treat batch with the same heat treatment as torsion fatigue specimens. Three M50 12.7 mm (1/2 in) diameter roughened steel balls,

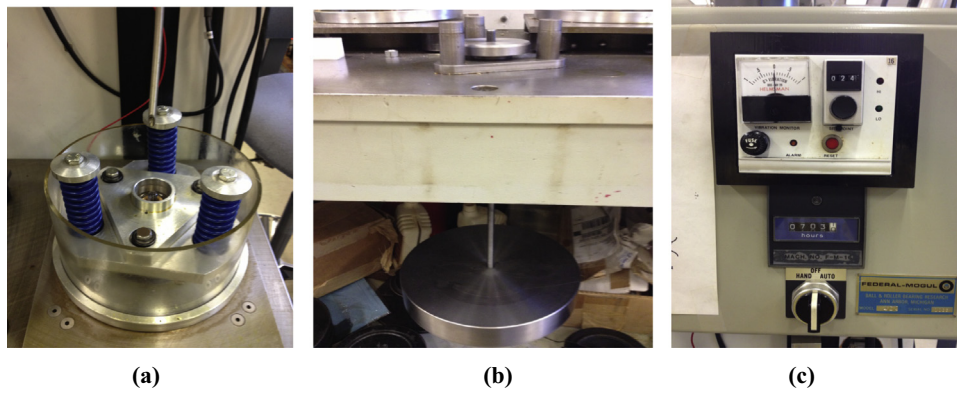


Fig. 9. Various parts of the 3-ball on rod rolling contact fatigue test rig. (a) Test head (one of four) with accelerometer, (b) loading mechanism and (c) vibration monitor system and time recorder.

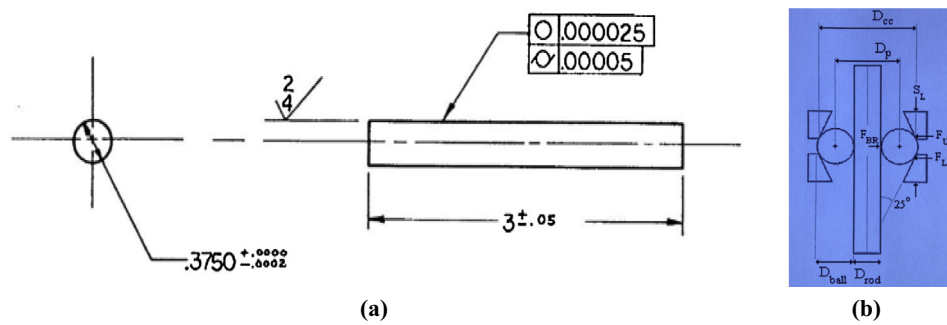


Fig. 10. Three-ball-on-rod RCF test specimen and loading configuration. (a) Dimensions of RCF rod (unit: inch) [21] and (b) loading schematic.

separated by a retainer, are radially loaded against the test specimen between two tapered cups thrust-loaded by three compression springs. The contact between the balls and rod configures a Hertzian contact. The test is conducted according to Glover [40].

3.2. Retained austenite and residual stresses measurement

X-ray diffraction was used to measure the levels of retained austenite and residual stresses in the torsion and rolling contact fatigue test specimens. The measurement was conducted using Bruker GADDS (General Area Detector Diffraction System).

The measurement of the volume fraction of retained austenite V_γ is according to ASTM E975-03 [41]:

$$V_\gamma = \left(\frac{1}{q} \sum_{j=1}^q \frac{I_{\gamma j}}{R_{\gamma j}} \right) / \left[\left(\frac{1}{p} \sum_{i=1}^p \frac{I_{\alpha i}}{R_{\alpha i}} \right) + \left(\frac{1}{q} \sum_{j=1}^q \frac{I_{\gamma j}}{R_{\gamma j}} \right) \right] \quad (13)$$

where I_α and I_γ represent the measured integrated intensities of ferrite and austenite, respectively. R_α and R_γ are structure-related parameters for ferrite and austenite, respectively. Their values are given in [41]. p and q are the numbers of ferrite and austenite peaks, respectively. In this study, $p = q = 3$.

The residual stresses measurement follows ASTM E2860-12 [42]. The details of measurement procedure can be found in [43].

4. Modeling results

4.1. Torsion fatigue tests result

As described in Section 2.4, torsion fatigue tests were carried out on carburized AISI 8620 steels with low and high RA content.

For each RA level three tests were conducted at different stress levels to obtain the S–N result, ultimate shear strength and endurance limit. Fig. 11 depicts the test results and the power law fit for both low and high RA cases. Using the procedure described in the previous section, the material parameters (i.e. m and τ_{r0}) for damage law were obtained and are given in Table 3.

Fig. 11 illustrates that the fatigue behavior of carburized AISI 8620 steel is significantly influenced by the level of RA. The material with high level of RA (~35%) exhibited a 40% increase in endurance limit as compared with the material having low level RA. The results demonstrate that retained austenite has a positive effect on the fatigue strength of carburized AISI 8620 steel. This is consistent with the experimental results of Zhu et al. [13] and Dommarco et al. [14].

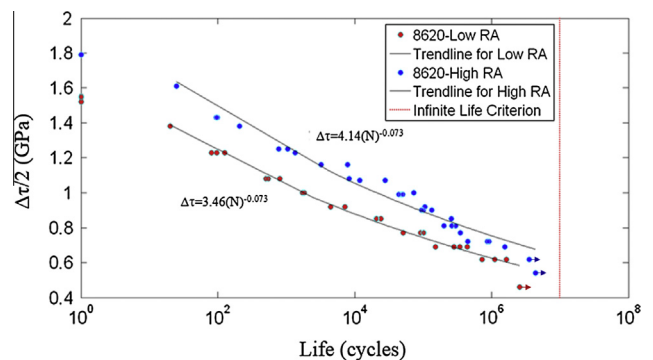


Fig. 11. S–N curves for carburized AISI 8620 steels (data point with arrow indicates run-out point).

Table 3

Material dependent parameters for carburized AISI 8620 steels with low and high retained austenite.

Parameters	S_{us} (GPa)	m	τ_{r0} (GPa)
Low RA	1.730	13.7	4.210
High RA	2.069	13.7	5.034

4.2. Effect of residual stresses on damage evolution

The internal residual stresses measurement showed that the field is compressive and nearly constant with a magnitude of 150 MPa, which is common in steels [44]. It is to be noted that the stress reversal $\Delta\tau$ is not affected by residual stresses, however, the residual stresses influence the damage evolution rate by affecting the mean component of stress σ_m in the denominator of Eq. (11). In the case with compressive residual stresses ($\sigma_m < 0$), the value of denominator is increased, thus $\frac{dD}{dN}$ is reduced, resulting in a slower damage accumulation and higher rolling contact fatigue life. This analysis agrees with the conclusion proposed by other researchers [6–12] that compressive residual stresses will elongate the fatigue life.

4.3. Simulation result

The ABAQUS FE damage mechanics based RCF model was used to investigate crack propagation pattern and final fatigue life of case carburized AISI 8620 steel with different levels of RA and RS. Figs. 12 and 13 illustrate the RCF life of carburized AISI 8620 steels with low and high retained austenite under 2.0 and 2.5 GPa loading, respectively. In order to obtain the probability of failure results of carburized AISI 8620 steels, the FE RCF model was used to simulate 33 different randomly generated Voronoi domains. Table 4 contains the slopes of the Weibull results shown in Figs. 12 and 13. The values of the Weibull slopes for this investigation are similar to those obtained by Jalalahmadi and Sadeghi [21]. Tables 5 and 6 list the fatigue life data extracted from Figs. 12 and 13. In both low and high RA cases, the fatigue lives of the material are increased by compressive residual stresses. It is to be noted that 150 MPa RS increases the fatigue life by about 16% while in 0.8 GPa RS case, the life increases by more than 50%. The L_{50} life of the low and high RA cases under the 2.0 GPa loading are in order of 10^8 and 10^9 cycles, respectively. The L_{50} life of the high RA simulation is almost one order of magnitude larger than that of the low RA case. A similar trend is observed for the loading condition of 2.5 GPa. The results show that with higher level of

retained austenite and compressive residual stresses, the fatigue life of carburized AISI 8620 steel will be improved.

Fig. 14 depicts the final fatigue spall shape and the corresponding damage evolution for the conditions without and with residual stresses. The cracks are located in RVE, forming a spall near the surface. The general spall shapes of both cases without and with residual stresses are similar, although little reduction in crack

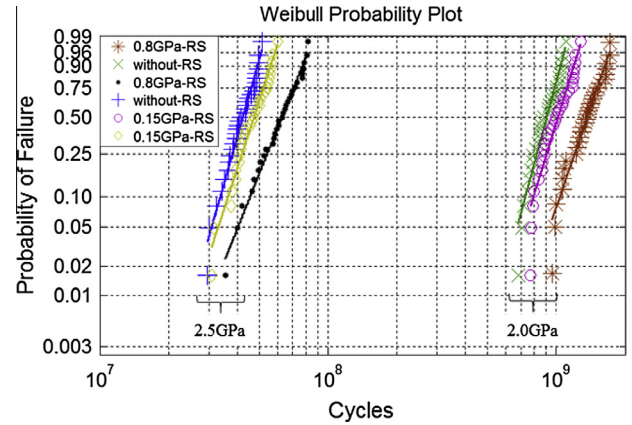


Fig. 13. Weibull plots for final fatigue lives of carburized AISI 8620 high retained austenite steel under 2.0 and 2.5 GPa Hertzian pressure.

Table 4

Weibull slopes for carburized AISI 8620 steel (low and high retained austenite cases).

Loading	RS type	Slopes of low RA case	Slopes of high RA case
2.0 GPa	Without RS	7.4	8.7
	0.15 GPa RS	6.5	7.6
	0.8 GPa RS	5.1	6.8
2.5 GPa	Without RS	8.8	8.2
	0.15 GPa RS	8.5	7.2
	0.8 GPa RS	6.3	5.9

Table 5

Average life extension for carburized AISI 8620 steel (low and high retained austenite cases).

RA type	Loading	RS type	Absolute extension of life ^a (10^6)	Relative extension of life ^b (%)
Low RA	2.0 GPa	0.15 GPa RS	11.3	15.6
		0.8 GPa RS	39.5	54.3
	2.5 GPa	0.15 GPa RS	1.6	16.5
		0.8 GPa RS	2.3	54.6
High RA	2.0 GPa	0.15 GPa RS	110	12.1
		0.8 GPa RS	440	48.7
	2.5 GPa	0.15 GPa RS	4.9	11.7
		0.8 GPa RS	20.0	47.6

^a Absolute extension of life = average life (with RS) – average life (without RS).

^b Relative extension of life = [average life (with RS) – average life (without RS)]/average life (without RS).

Table 6

L_{50} life for carburized AISI 8620 steel (low and high retained austenite cases).

Loading	RS type	Low RA L_{50} (10^6)	High RA L_{50} (10^6)
2.0 GPa	Without RS	76	900
	0.15 GPa RS	85	1000
	0.8 GPa RS	103	1050
2.5 GPa	Without RS	3.9	42
	0.15 GPa RS	4.2	48
	0.8 GPa RS	5.8	64

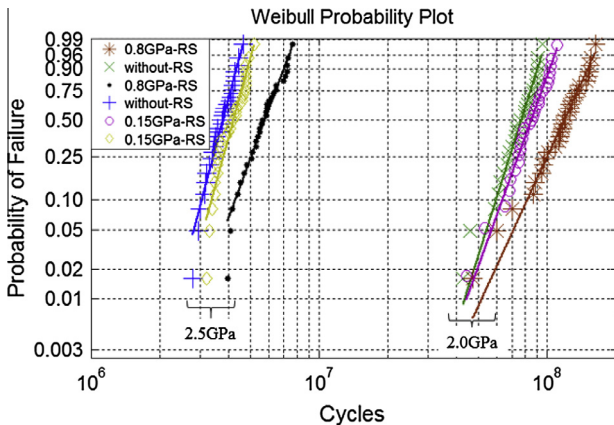


Fig. 12. Weibull plots for final fatigue lives of carburized AISI 8620 low retained austenite steel under 2.0 and 2.5 GPa Hertzian pressure.

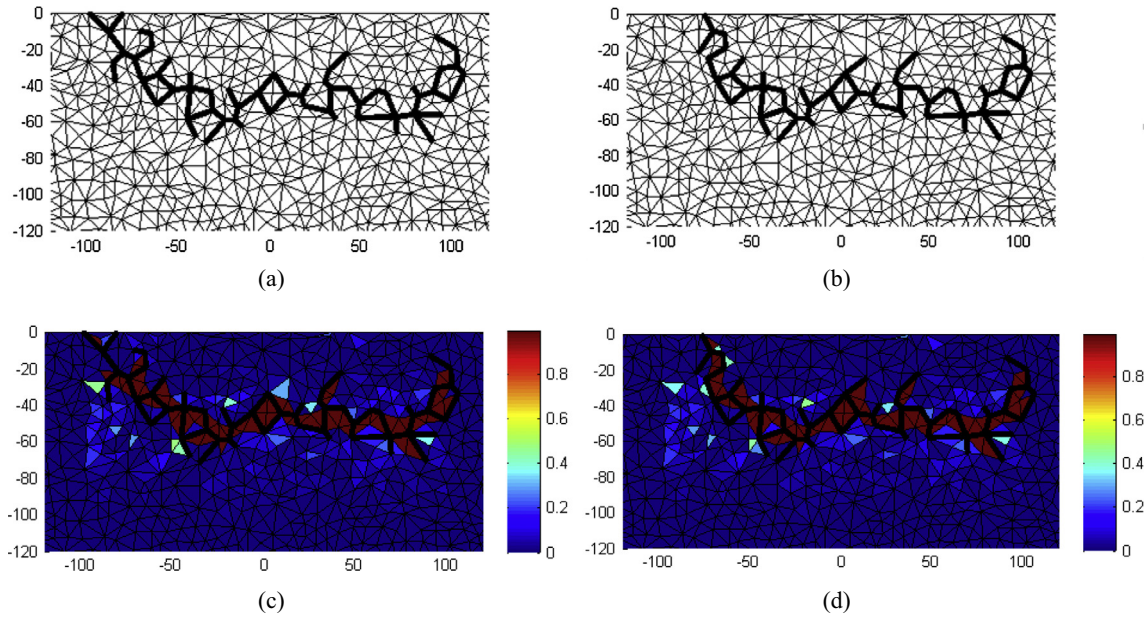


Fig. 14. Spall shapes and damage conditions of cases without and with RS. (a) Spall shape (without RS), (b) spall shape (with 0.8 GPa RS), (c) damage condition (without RS), (d) damage condition (with 0.8 GPa RS)

branches due to residual stresses is observed. The fatigue damage conditions in the two cases are also similar. However, the fatigue life of the case with 0.8 GPa residual stresses is extended by about 50% compared to the case without residual stresses. The results demonstrate that the compressive residual stresses delay the damage evolution but have little influence on the final shape of spall configuration. This idea is also supported by Webster [45], who suggested that compressive residual stresses decelerate the initiation and growth phases of the fatigue process.

5. Experimental results & verification

The three-ball-on-rod RCF tests were conducted to determine the probability of failure of case carburized AISI 8620 steel with different levels of RA and corroborate with the numerical results. Internal material flaws exist in bearing steels due to improper bonding between inclusions and base material matrix [31]. To better understand and corroborate the simulation and experimental results, flaws were modeled as broken interfaces between adjoining elements. In this investigation, similar to the work of Raje et al. [31], five random initial flaws were introduced in each domain. Fig. 15 illustrates the RCF experimental results for the low and high RA carburized AISI 8620 steels as well as the corresponding simulation results (with flaws) under 2.0 GPa Hertzian loading. The Weibull slopes of both numerical (marked as e_A) and test results (marked as e_T) are also shown in Fig. 15. The slopes of the experimental results are 1.70 and 1.68 for low and high RA cases, respectively, which are both within the range 0.51–5.7 as discussed by Harris and Barnsby [46]. Table 7 contains the results of fatigue lives shown in Fig. 15. For both the low and high RA cases, the L_{10} , L_{50} and L_{90} lives of simulation results compare well with the three-ball-on-rod experimental result. Compared to the experimental L_{50} life for low RA specimens which is about 40 million cycles, the life of specimens with high RA content is almost three times larger, indicating again that higher level of retained austenite results in higher RCF life of carburized AISI 8620 steel. Similar phenomenon is observed for L_{10} and L_{90} life. Table 8 shows the L_{50} life of simulation results in this study and the experimental result obtained from Hanejko et al. [47] under

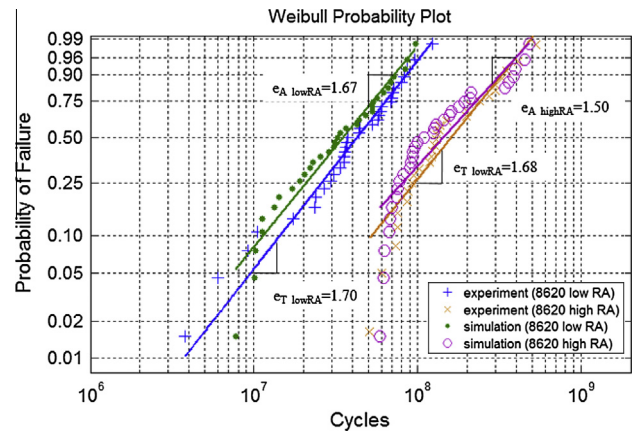


Fig. 15. Experimental and numerical Weibull plots for fatigue lives of carburized AISI 8620 low and high RA steels.

Table 7

Fatigue lives of carburized AISI 8620 low and high retained austenite steel under 2.0 GPa loading (experiment and simulation).

RA type	Cases	L_{10} (10^6)	L_{50} (10^6)	L_{90} (10^6)
Low RA	Experiment	16	42	85
	Simulation	12	36	73
High RA	Experiment	50	170	340
	Simulation	40	150	330

Table 8

L_{50} life of carburized AISI 8620 steel under 2.5 GPa loading (experiment and simulation).

Cases	L_{50} (10^6)
Experiment [47]	4.2
Simulation (with 0.15 GPa RS)	4.2

2.5 GPa loading. The simulation and experimental results match well. Overall, the fatigue lives obtained from the RCF model well reflect the experimental results.

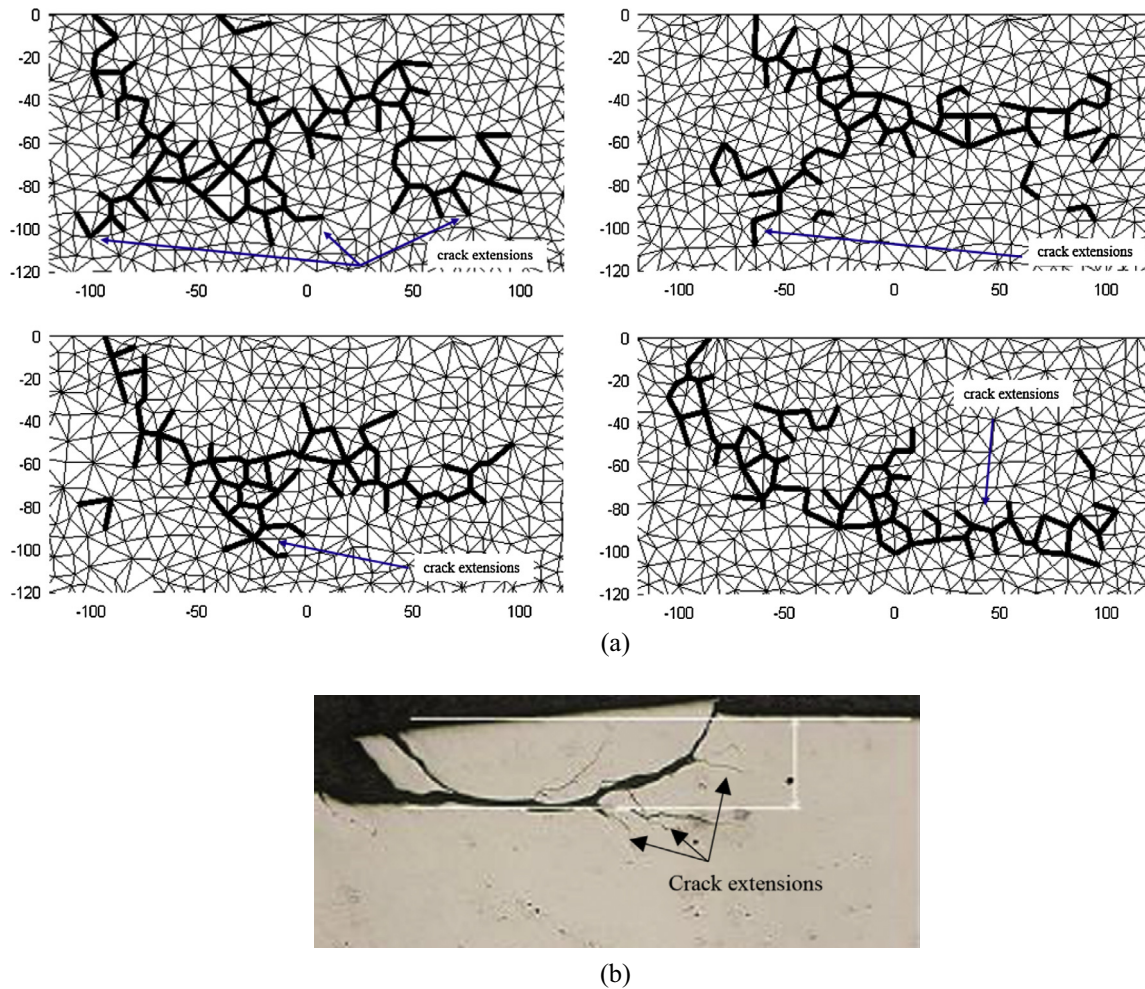


Fig. 16. Numerical and experimental spalling patterns of carburized AISI 8620 steel. (a) Simulated spalling patterns of carburized AISI 8620 steel (unit: μm) and (b) subsurface spalling pattern observed in carburized AISI 8620 steel [47].

Fig. 16a depicts the simulated spall for several domains. Besides the general spall shapes which is similar to Fig. 14, there are several crack extensions below the spall due to the presence of initial flaws. This phenomenon correlates well with the experimental RCF results of Hanjeko et al. [47], which is illustrated in Fig. 16b. The experimental observation also demonstrates several extended cracks connected with the general spall.

6. Conclusion

This paper numerically and experimentally investigates the rolling contact fatigue behavior of carburized AISI 8620 steels with different amounts of retained austenite and residual stresses. A two dimensional RCF model based on damage mechanics was developed. The effects of residual stresses were incorporated into the damage evolution rate. Experimental torsion fatigue tests were conducted and the results were used to obtain material parameters to calibrate the RCF model. Three-ball-on-rod RCF tests were conducted to study fatigue life under actual RCF condition and investigate the scatter in life data.

The simulation results showed that the presence of compressive residual stresses in carburized AISI 8620 steel is beneficial and increases the RCF life. The compressive residual stresses reduce the damage evolution rate however, negligibly affect the spall shape. The spalling pattern in the simulation compares well with the experimental observation. The combined results from torsion fatigue tests, three-ball-on-rod RCF tests and simulation indicated

that higher amounts of retained austenite results in a higher RCF life of carburized AISI 8620 steel. Corroboration of experimental and numerical results indicates that the developed RCF model successfully predicts the rolling contact fatigue life of carburized AISI 8620 steel with different levels of retained austenite and residual stresses.

Acknowledgements

The authors would like to express their deepest appreciations to the Cummins Inc. for their support of this project.

References

- [1] Littmann WE, Widner RL. Propagation of contact fatigue from surface and sub-surface origins. *ASME J Basic Eng* 1966;88:624–36.
- [2] Weinzapfel N, Sadeghi F. Numerical modeling of sub-surface initiated spalling in rolling contacts. *Tribol Int* 2013;59:210–21.
- [3] Lundberg G, Palmgren A. Dynamic capacity of roller bearings. *Acta Polytech, Mech Eng Series* 1952;2(4):1–32.
- [4] Sadeghi F, Jalalahmadi B, Slack TS, Raju N, Arakere NK. A review of rolling contact fatigue. *J Tribol* 2009;131(4).
- [5] Manoj V, Manohar Shenoy K, Gopinath K. Developmental studies on rolling contact fatigue test rig. *Wear* 2008;264(7–8):708–18.
- [6] Cretu SS, Benchea MI. Compressive residual stresses effect on fatigue life of ball bearings. *ASME international mechanical engineering congress and exposition*; 2007.
- [7] Chen Q, Hahn GT, Rubin CA, Bhargava V. The influence of residual stresses on rolling contact mode II driving force in bearing raceway. *Wear* 1988;26:17–30.
- [8] Guo Y. Modeling of rolling contact fatigue for hard machined components with process-induced residual stress. *Int J Fatigue* 2004;26(6):605–13.

- [9] Choi Y, Liu CR. Rolling contact fatigue life of finish hard machined surfaces: part 1. Model development. *Wear* 2006;261:485–91.
- [10] Choi Y, Liu CR. Rolling contact fatigue life of finish hard machined surfaces: part 2. Experimental verification. *Wear* 2006;261:492–9.
- [11] Liu CR, Choi Y. Rolling contact fatigue life model incorporating residual stress scatter. *Int J Mech Sci* 2008;50(12):1572–7.
- [12] Prevey P, Jayaraman N. Introduction of residual stress to enhance fatigue performance in the initial design. *Turbo Expo* 2004;513:7–9.
- [13] Zhu D, Wang FX, Cai QC. Effect of retained austenite on rolling element fatigue and its mechanism. *Wear* 1985;105:223–34.
- [14] Dommarco RC, Kozaczek KJ, Bastias PC, Hahn GT, Rubin CA. Residual stresses and retained austenite evolution in AISI 52100 steel under non-ideal rolling contact loading. *Wear* 2004;257(11):1081–8.
- [15] Zheng C, Dan R, Zhang F, Lv B, Yan Z, Shan J, et al. Effects of retained austenite and hydrogen on the rolling contact fatigue behaviours of carbide-free bainitic steel. *Mater Sci Eng, A* 2014;594:364–71.
- [16] Silva VF, Canale LF, Spinelli D, Crnkovic OR. Influence of retained austenite on short fatigue crack growth and wear resistance of case carburized steel. *J Mater Eng Perform* 1999;8(October):543–8.
- [17] Prado JM, Arques JL. Influence of retained austenite on the fatigue endurance of carbonitrided steels. *J Mater Sci* 1984;19:2980–8.
- [18] Abareshi M, Emadoddin E. Effect of retained austenite characteristics on fatigue behavior and tensile properties of transformation induced plasticity steel. *Mater Des* 2011;32(10):5099–105.
- [19] Hu Z, Ma M, Liu Y, Liu J. The effect of austenite on low cycle fatigue in three-phase steel. *Int J Fatigue* 1997.
- [20] Herring D. A discussion of retained austenite, *The Heat Treat Doctor*; 2005.
- [21] Jalalahmadi B, Sadeghi F. A Voronoi finite element study of fatigue life scatter in rolling contacts. *ASME J Trib* 2009;131(2).
- [22] Bomidi JAR, Weinzapfel N, Slack T, Mobasher Moghaddam S, Sadeghi F, Liebel A, et al. Experimental and numerical investigation of torsion fatigue of bearing steel. *ASME J Tribol* 2012.
- [23] Mobasher Moghaddam S, Bomidi JAR, Sadeghi F, Weinzapfel N, Liebel A. Effects of compressive stresses on torsional fatigue. *Tribol Int* 2014;77:196–210.
- [24] Bomidi JAR, Weinzapfel N, Sadeghi F, Liebel A, Weber J. An improved approach for 3d rolling contact fatigue simulations with microstructure topology. *Tribol Trans* 2013;56(3):385–99.
- [25] Warhadpande A, Jalalahmadi B, Slack T, Sadeghi F. A new finite element fatigue modeling approach for life scatter in tensile steel specimens. *Int J Fatigue* 2010;32:685–97.
- [26] Warhadpande A, Sadeghi F. Effect of surface defects on rolling contact fatigue of heavily loaded lubricated contacts. *Proc Institution Mech Eng, Part J: J Eng Tribol* 2010;224(10):1061–77.
- [27] Lemaitre J, Plumtree A. Application of damage concepts to predict creep-fatigue failures. *J Eng Mat Technol Trans ASME* 1979;101:248–92.
- [28] Lemaitre J. Local approach of fracture. *Eng Fracture Mech* 1986;25:523–37.
- [29] Xu G, Sadeghi F. Spall initiation and propagation due to debris denting. *Wear* 1996;201:106–16.
- [30] Xu G, Sadeghi F, Cogdell JD. Debris denting effects on elastohydrodynamic lubricated contacts. *ASME J Tribol* 1997;119:579–87.
- [31] Raje N, Sadeghi F, Rateick RG. A statistical damage mechanics model for subsurface initiated spalling in rolling contacts. *J Tribol* 2008;130(4):042201.
- [32] Slack T, Sadeghi F. Explicit finite element modeling of subsurface initiated spalling in rolling contacts. *Tribol Int* 2010;43:1693–702.
- [33] Kachanov LM. On creep rupture time. *Lzv Acad Nauk SSSR Otd Technol Nauk* 1958;8:26–31.
- [34] Xiao Y, Li S, Gao Z. A continuum damage mechanics model for high cycle fatigue. *Int J Fatigue* 1998;20(7):503–8.
- [35] Basquin OH. The exponential law of endurance tests. *Am Soc Testing Mater Proc* 1910;10:625–30.
- [36] Ince A, Glinka G. A modification of Morrow and Smith-Watson-Topper mean stress correction models. *Fatigue Fract Eng Mater Struct* 2011;34(11):854–67.
- [37] Bower F. Applied mechanics of solids. Chapter 9, Modeling material failure; 2008.
- [38] Lemaitre J. A course on damage mechanics. Berlin: Springer-Verlag; 1992.
- [39] International Organization for Standardization (ISO), Metallic materials-Torque-controlled fatigue testing, ISO 1352: 2011(E), second ed., 2011, 04–15.
- [40] Glover D. A ball-rod rolling contact fatigue tester. In: Hoo JJC, editor. Rolling Contact Fatigue Testing of Bearing Steels, ASTM STP 771. American Society for Testing and Materials; 1982. p. 107–24.
- [41] Standard practice for X-ray determination of retained austenite in steel with near random crystallographic orientation, ASTM E975-03; 2003.
- [42] Standard test method for residual stress measurement by X-ray diffraction for bearing steels, ASTM E2860-12; 2012.
- [43] Hilley ME, editor. Residual stress measurement by X-ray diffraction, SAE J784A. Society of Automotive Engineers; 1971. p. 21–4.
- [44] Van Wijk S, François M, Sura E, Frabolot M. Retained austenite and residual stress evolution in carbonitrided shot-peened steel. *Mater Sci Forum* 2011;681:374–80.
- [45] Webster GA, Ezeilo AN. Residual stress distributions and their influence on fatigue lifetimes. *Int J Fatigue* 2001;23:375–83.
- [46] Harris TA, Barnsby RM. Life rating for ball and roller bearings. *J Eng Tribol* 2001;215:577–95.
- [47] Hanejko F, Rawlings A, Narasimhan KSV. Surface densified P/M steel – comparison with wrought steel grades, Euro PM2005, Prague; 2005. p. 509–511.